

Unfolding the Atmospheric Muon Flux with IceCube: Investigating Stopping Muons and High-Energy Prompt Contributions

The IceCube Collaboration

(a complete list of authors can be found at the end of the proceedings)

E-mail: pascal.gutjahr@tu-dortmund.de, lucas.witthaus@tu-dortmund.de

Atmospheric muons produced in cosmic-ray air showers are classified as conventional muons from pion and kaon decays and prompt muons from heavy hadron decays. Conventional muons dominate at lower energies, and the prompt component becomes dominant at PeV energies and above. Precisely measuring the atmospheric muon flux from a few GeV to several PeV is valuable for advancing our understanding of cosmic-ray interactions and testing hadronic interaction models. Low-energy muons that stop within the IceCube in-ice array provide valuable information about the energy spectrum of muons from a few hundred GeV up to 10 TeV. Machine learning techniques are employed to enhance event reconstruction and selection to provide insights into the conventional and prompt components. This contribution presents the unfolding of the energy spectrum of stopping muons in IceCube as well as the unfolding of high-energy muons to probe the prompt component.

Corresponding authors: Pascal Gutjahr^{1,2*}, Lucas Witthaus^{1,2}

¹ *Dept. of Physics, TU Dortmund University*

² *Lamarr Institute for Machine Learning and Artificial Intelligence*

* Presenter

39th International Cosmic Ray Conference (ICRC2025)
15–24 July 2025
Geneva, Switzerland



1. Introduction

Atmospheric muons, generated by cosmic-ray interactions with Earth’s atmosphere, serve as powerful probes for investigating particle physics phenomena beyond the reach of current collider experiments. They are typically classified into conventional muons, originating predominantly from the decay of charged pions and kaons, and prompt muons, arising from the decay of heavy mesons containing charm and other heavy quarks [1]. While conventional muons dominate the muon flux at energies up to several hundred TeV, the prompt component becomes increasingly relevant at PeV energies and beyond. Precisely characterizing these muon fluxes across a broad energy spectrum is essential to refine hadronic interaction models. It also addresses outstanding questions in cosmic-ray physics, including the longstanding “muon puzzle” [2], an unexplained discrepancy between the observed and expected muon production rates of GeV muons — increasing towards high primary particle energies.

The IceCube Neutrino Observatory [3] embedded deep within the Antarctic ice, provides a unique opportunity to measure the atmospheric muon flux over a wide energy range. Building on previous work [4], this study leverages both low-energy stopping muons, which halt within the IceCube in-ice array, and high-energy muons penetrating through the detector, to comprehensively unfold the muon energy spectrum. Stopping muons, spanning energies from hundreds of GeV to approximately 10 TeV, are particularly valuable as they allow detailed studies of muon propagation through the ice and aid in refining our understanding of the underlying hadronic interaction processes in the atmosphere. High-energy muons provide access to the prompt muon flux, enabling the study of charmed meson production at energies and forward directions otherwise inaccessible due to collider limitations.

This work employs convolutional neural networks (CNNs) to reconstruct and select events in order to perform the unfolding and provide critical insights into atmospheric muon production mechanisms.

2. Event Selection

2.1 Event Reconstruction

The machine learning algorithms are trained on Monte Carlo (MC) generated muons resulting from air-showers simulated with CORSIKA 7 [5]. Both the reconstruction of stopping muons and high-energy muons is performed using the deep learning framework described in [6]. Neural networks are applied to reconstruct the events based on the measured Cherenkov light pulses in the IceCube in-ice array. The pulses are used to define network input features from each of the digital optical modules: the total charge, the time of the first pulse, and the charge-weighted standard deviation of the pulse arrival times. Due to the distinct geometrical configurations of the three sub-arrays constituting the detector (main array, lower and upper DeepCore), the data is transformed to an orthogonal grid and fed into separate convolutional layers. The results are flattened and passed into two fully connected sub-networks which perform the parameter estimation as well as a per-event uncertainty estimation for each parameter. During training, the network’s weights and biases are adjusted to minimize a loss function in form of a multivariate Gaussian. The networks predict the muon’s direction, stopping point, detector entry point, energy deposited in the detector,

energy of the most energetic muon of the muon bundle entering the detector (referred to as leading muon) and the energy of the muon bundle at surface. This information is used to perform a selection of stopping and high-energy muons, and they finally serve as an input to unfold the muon energy spectrum and depth intensity. The exact cuts defining the selections are given in [Table 1](#).

2.2 Stopping Muons

Atmospheric stopping muons are defined as muons which decay inside the IceCube in-ice array. By this point, these muons will have lost most of their initial energy through interactions in the ice. The coordinates of the stopping point can be retrieved, as it is located within the instrumented volume. This, together with the direction, enables the computation of the muon's propagated length through the ice. The length in turn correlates with the muon energy at the surface. In case of a stopping muon event with multiple muons reaching the in-ice array, IceCube is not able to distinguish them separately. However, the visible track corresponds to the muon with the highest energy because it propagates over the longest distance. For the stopping muon selection, an additional classification score is predicted to determine whether an event is a stopping event. The selection is defined by imposing a cut on the classification score, along with additional quality cuts on the per event uncertainties of the neural network reconstructions.

2.3 Leading Muons

Towards energies above ~ 10 TeV, the muons within the bundles are too energetic to stop inside the in-ice array of IceCube. Hence, the muon bundle transverses the detector. The leading muon is used to infer the high-energy muon flux at surface. Above 10 TeV, the leading muon is expected to dominate the bundle, carrying the vast majority of its energy [7]. Obviously, the higher the energy of the leading muon, the higher the energy of the muons at surface level. Machine learning techniques are used to reconstruct only the leading muon energy in the muon bundle. This is motivated by stochastic energy losses. A muon bundle with a leading muon that dominates the bundle deposits its energy more stochastically than a bundle with many muons carrying a similar amount of energy, where all the losses sum up and result to a smoother loss along the muon track [7]. To improve the resolution of this reconstruction, events where the leading muon carries at least 40 % of the entire bundle energy at the entry of the detector (referred to as leadingness), are selected. This cut was optimized to improve data–MC of the leading muon reconstruction. Due to the large amount of events in the lower energy region, a cut of 500 TeV on a predicted muon bundle energy at the surface is applied to remove events below ~ 10 TeV muon energy at surface. To reduce the background of neutrinos in the sample, only events with $\cos(\theta) > 0.2$ are kept. Also, data–MC quality cuts are performed on the several properties and uncertainty estimations.

3. Unfolding

Experiments are typically conducted to find the distribution of a physical quantity $f(x)$. However, this distribution often cannot be determined directly. The experiment is only capable of measuring variables y that are correlated to a physical quantity of interest. These variables are referred to as observables and can be seen as the response of the detector to the underlying physical truth. *Unfolding* refers to the method of inverting this measurement process, thus finding the most

Table 1: Overview of all applied cuts to build the leading and stopping muon sample. Cuts are categorized into classification, uncertainty, containment and neutrino veto to select stopping and leading muons with sufficient data–MC agreement.

Cut Type	Feature	>	<
Stopping Muons			
Classification	classification score	0.99	
Uncertainty	zenith stopping depth		0.1 rad 60 m
Leading Muons			
Containment	length in detector	1000 m	2000 m
	entry pos x, y	−750 m	750 m
	entry pos z	−500 m	750 m
	center pos x, y	−550 m	550 m
	center pos z	−650 m	650 m
Neutrino Veto	$\cos(\theta)$	0.2	
	length	5000 m	15000 m
Classification	leadingness	0.4	
Uncertainty	bundle energy at entry		$0.9 \log_{10}(\text{GeV})$
	bundle energy at surface		$2.0 \log_{10}(\text{GeV})$
	zenith		0.1 rad
	azimuth		0.2 rad
	entry pos x, y, z		42 m
	center pos x, y, z		50 m
	entry pos time		200 ns
	center pos time		600 ns
	length in detector		160 m
	length		2000 m

probable distribution $f(x)$ based on the measurement $g(y)$ [8]. The distribution of the true variable $f(x)$ is connected to the observable distribution $g(y)$ via the *Fredholm integral equation* [9]

$$g(y) = \int A(x, y) f(x) dx + b(y). \quad (1)$$

The detector response function $A(x, y)$ describes the entire detection process and is usually obtained from MC simulations. It contains the probability of measuring an observable value y if the value of the true variable is x . The term $b(y)$ accounts for background contributions and can be neglected for the sufficiently pure sets in this analysis. Discretizing Equation 1 and assuming a Poisson distribution for each bin of the observed distribution \mathbf{g} allows to construct a likelihood of the form.

$$l(\mathbf{f}|\mathbf{g}) = \sum_i \left((\mathbf{A} \cdot \mathbf{f})_i - g_i \ln((\mathbf{A} \cdot \mathbf{f})_i) \right) + \tau^{-1} \mathcal{R}(\mathbf{f}). \quad (2)$$

The *Tikhonov regularization* [10] term $\mathcal{R}(\mathbf{f})$ is added to the likelihood to suppress oscillating solutions for the vector \mathbf{f} . The parameter τ controls the regularization strength. Small values

cause strong regularization with a flat spectrum, whereas large values lead to a comparably small penalty term that leaves the initial likelihood almost unchanged. Similar to Ref. [8], the optimal τ is expected to minimize the total correlation ρ between the components of the solution vector \mathbf{f} , defined as the sum of off-diagonal elements V_{ij} of its covariance matrix \mathbf{V}

$$\rho = \sum_{i>j} V_{ij}. \quad (3)$$

It is determined via a grid search over a predefined range of τ values.

The statistical uncertainties are estimated by evaluating the inverse of the Hessian matrix at the likelihood minimum, which approximately describes the covariance matrix of the fit parameters. Systematic uncertainties are incorporated into the solution by modeling them as nuisance parameters. Using the SnowStorm method in IceCube [11], the bin counts in observable space are fitted by linear weighting functions $w_{j,i}$, which quantify the effect of changes in a systematic parameter j on bin i . They are taken into account in the detector response matrix

$$\mathbf{A}' = \mathbf{w}_j^T \cdot \mathbf{A}, \quad (4)$$

which allows to minimize the likelihood with respect to those additional parameters.

4. Results

To demonstrate the consistency of the network reconstructions of stopping muons, the data–MC agreement for the reconstructed stopping depth and the cosine zenith angle is presented in Fig. 1. The stopping depth ranges from 1650 m to 2450 m and the data agrees well with the MC. The distribution shows a feature around 1950 m, likely due to the dust layer in IceCube. It is a region between 2000 m and 2100 m depth with increased scattering and absorption due to high dust concentration [3]. The network estimates larger uncertainties in this region because it is challenging to distinguish between truly stopping muons and those that enter the dust layer, which produce no additional signal in the detector due to the absorption of the Cherenkov light. As a result, many events are removed by the quality cuts in this region. The cosine zenith distribution ranges from 0–1 with good agreement above 0.4. From 0.2–0.4, there are larger fluctuations caused by limited statistics towards the horizon. Since atmospheric muons cannot transverse an infinite path through a dense medium, an increasing amount of events is expected to arise from neutrino-induced muons in this region. However, the effect is negligible, as presented in Fig. 1b. Since an offset of the total normalization between data and MC is expected [2], the MC normalization is scaled by a factor 1.10 to fit the number of data events in the selected sample. The factor is determined by dividing the number of detected events by the number of expected MC events. Scaling has no impact on the unfolding because the columns of the detector response matrix in Equation 2 are normalized.

The unfolding procedure is further validated on MC data to ensure its robustness and model independence utilizing stopping muons. The method is applied to a data set with a fixed primary flux model, using training data from the four different flux models (H3a [13], H4a [13], GST [14], GSF [15]). Figure 2 shows that the unfolded distributions consistently reproduce the true test distribution, regardless of the training model. This confirms that the method is not overly sensitive to the choice of training model and can generalize well to unseen data.

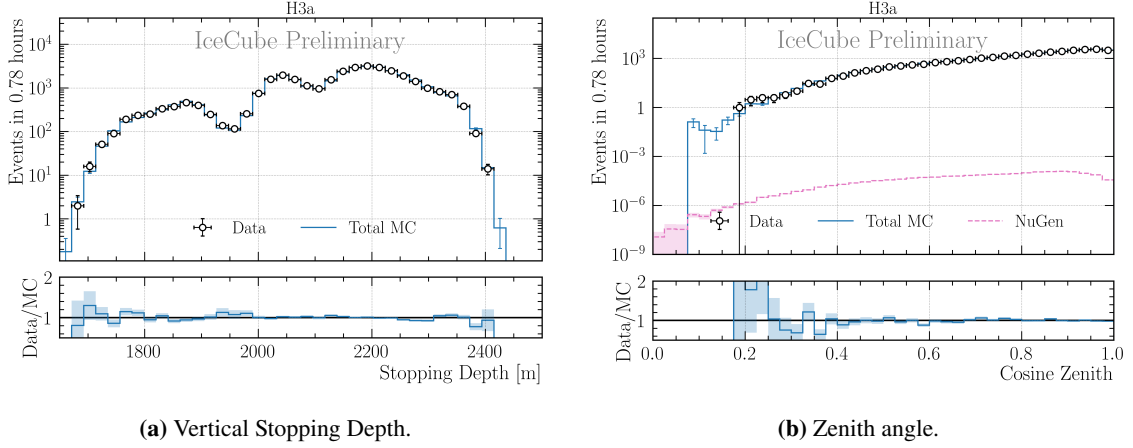


Figure 1: Data–MC agreement for the reconstruction of the vertical stopping depth and the zenith angle. To match the total number of MC events with data, CORSIKA is up-scaled by a factor of 1.10. Neutrino simulation (NuGen) estimates the background assuming a single power law [12].

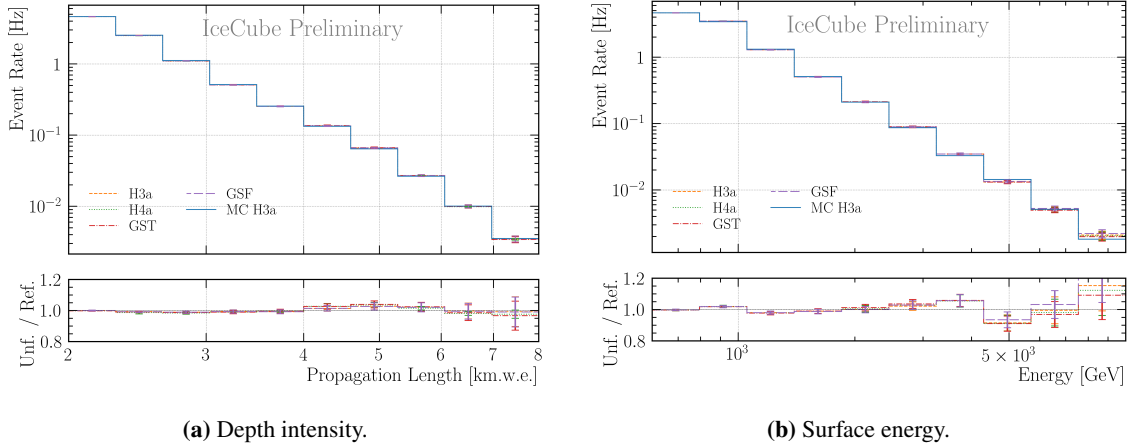
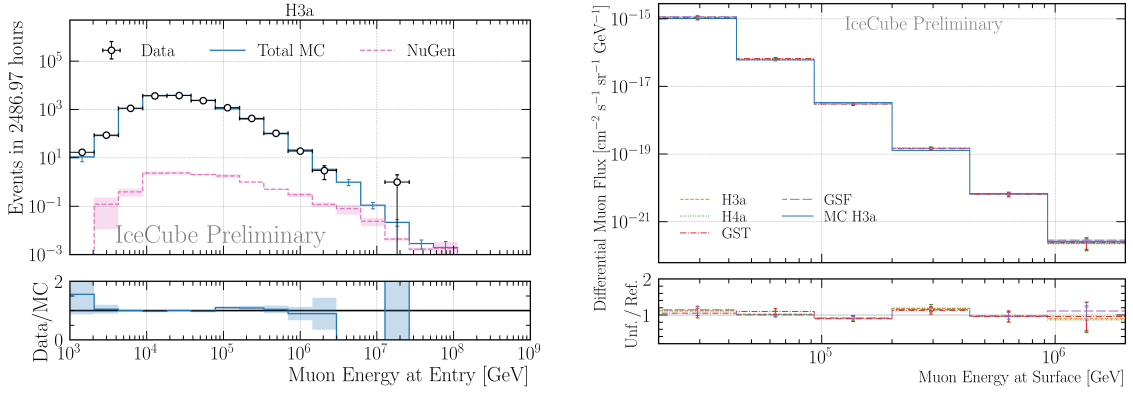


Figure 2: Model dependence of the unfolding procedure on MC data. The unfolding is trained on on four different models (H3a [13], H4a [13], GST [14], GSF [15]), to unfold a test set with H3a as a fixed primary model. All results show good agreement with the injected true spectrum. They are well contained within the uncertainties.

Similar to the stopping muons, the data–MC agreement and the robustness test is presented for the leading muons in Fig. 3. A scaling factor of 1.12 is applied. The factor differs slightly to the one of the stopping muons, since it depends on the event selection. The robustness test is performed for the three models H4a, GST and GSF. For all models, the deviations are within the uncertainties.

With the method validated on MC, it is subsequently applied to IceCube data to unfold the depth intensity and surface energy spectra. The depth intensity of 32 943 events from 0.78 h of IceCube data is shown in Fig. 4a together with the prediction of MUTE (MUon inTensity codE) [16] for ice with a density of 0.917 g/cm^3 . MUTE is a computational tool for calculating atmospheric muon fluxes and intensities underground by combining surface flux predictions with muon propagation through matter. The unfolded results are shown with combined statistical and



(a) Data–MC agreement is shown for the reconstruction of the leading muon energy at the entry of the detector. Total MC includes the CORSIKA simulation and the neutrino simulation (NuGen) to estimate the background assuming a single power law [12]. To match the total number of MC events with data, CORSIKA is up-scaled by a factor of 1.12.

(b) Model dependence of the unfolding procedure on MC data. The unfolding is trained on three different models (H4a [13], GST [14], GSF [15]), to unfold a test set with H3a [13] as a fixed primary model.

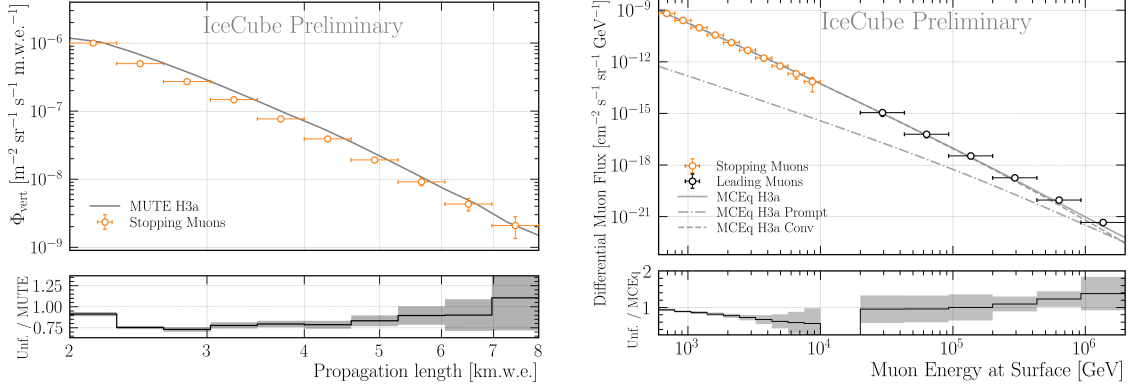
Figure 3: Model dependence test and data–MC agreement are presented for leading muons.

systematic uncertainties, which also account for deviations in the effective area caused by varying the ice systematics. For propagation lengths between (2.5 – 5.5) km.w.e., the vertical muon flux is about 20 % lower than expected. This comparison indicates a dependence of the discrepancies on the propagation length.

The unfolding of the differential muon flux as a function of the muon energy at surface is presented in Fig. 4b, utilizing both stopping muons for the low-energy flux, and leading muons for the high-energy flux. The leading muon unfolding uses 2486.97 h of IceCube data (12754 events). The distribution of stopping muons agrees with MCEq calculations at about 600 GeV, but start to disagree with a slope towards 10 TeV. The leading muon flux agrees with MCEq from 20 TeV to 200 TeV. At higher energies, the measured spectrum appears harder, indicating an excess of muons, however the uncertainties are within the prediction. A difference between the MCEq prediction and the CORSIKA simulation is the hadronic interaction model. MCEq utilizes SIBYLL 2.3c [17], CORSIKA simulations utilize SIBYLL 2.3d [18].

5. Conclusion & Outlook

Machine learning methods are utilized to select stopping muons in IceCube, and to reconstruct direction and energy of stopping and leading muons. The shapes of the data agree well with MC for all reconstructed properties. However, a scaling factor of 1.10 for stopping muons, and 1.12 for leading muons, needs to be applied to match a global offset. An unfolding approach is used to estimate the muon flux as a function of the propagation length, and as a function of the energy at surface. Robustness tests are performed by building the unfolding matrix based on different cosmic-ray primary mass compositions. The variations are within the uncertainties.



(a) Unfolded depth intensity obtained from 0.78 h of IceCube data together with the prediction from MUTE [16]. Ratio shows the unfolded result to the MUTE prediction.

(b) Unfolded muon flux at surface obtained from 2486.97 h of IceCube data together with predictions from MCEq. Ratio shows the unfolded result to MCEq prediction.

Figure 4: Unfolded depth intensity and muon flux at surface utilizing stopping muons and leading muons.

The unfolded propagation length with 0.78 h of IceCube data, is compared to a calculation by the tool MUTE. Between 2.5 km.w.e. and 5.5 km.w.e., the measured flux is about (10 – 20) % lower than the prediction. This could potentially caused by not sufficiently described energy losses in the muon propagation simulation. The unfolded muon energy at surface utilizing both stopping muons and leading muons (with 2487 h of data) is compared to numerical calculations by MCEq. For the stopping muons, the unfolded flux is below the prediction and decreasing towards 10 TeV. The measured leading muon flux is in good agreement with the prediction from MCEq within the uncertainties. At energies around (1 – 2) PeV, the prediction indicates that the prompt and conventional components contribute approximately equally to the total muon flux. After finalizing the analysis, it is planned to use 12 years of IceCube data for the leading muon flux unfolding, to extend the unfolded energy range to the point where the prompt component becomes dominant.

References

- [1] L. Neste *et al.*, *The European Physical Journal C* **85** no. 7, (2025) 759.
- [2] J. Albrecht *et al.*, *Astrophysics and Space Science* **367** no. 3, (Mar., 2022) 27.
- [3] **IceCube** Collaboration, *JINST* **12** no. 03, (2017) P03012.
- [4] **IceCube** Collaboration, *Astroparticle Physics* **78** (May, 2016) 1–27.
- [5] D. Heck *et al.*, “CORSIKA: A Monte Carlo code to simulate extensive air showers,” Technical Report FZKA 6019, Forschungszentrum Karlsruhe, 1998.
- [6] **IceCube** Collaboration, *Journal of Instrumentation* **16** (2021) P07041.
- [7] M. Aartsen *et al.*, *Astroparticle Physics* **78** (2016) 1–27.
- [8] V. Blobel *et al.*, *Statistische und numerische Methoden der Datenanalyse*. Teubner Studienbücher Physik, 1998.
- [9] I. Fredholm, *Acta Mathematica* **27** (1903) 365–390.
- [10] A. N. Tikhonov, *Proceedings of the USSR Academy of Sciences* **39** (1943) 195–198.
- [11] M. Aartsen *et al.*, *Journal of Cosmology and Astroparticle Physics* **2019** no. 10, (Oct, 2019) 048.
- [12] **IceCube** Collaboration, *PoS ICRC2023* (2023) 1064.
- [13] T. K. Gaisser, *Astroparticle Physics* **35** no. 12, (2012) 801–806.
- [14] T. K. Gaisser *et al.*, *Frontiers of Physics* **8** (2013) 748–758.
- [15] H. Dembinski *et al.*, *PoS ICRC2017* (2017) 533.
- [16] W. Woodley *et al.*, *Phys. Rev. D* **110** no. 6, (2024) 063006.
- [17] F. Riehn *et al.*, *Physical Review D* **100** no. 10, (2019) 103018.
- [18] F. Riehn *et al.*, *Phys. Rev. D* **102** no. 6, (2020) 063002.

Full Author List: IceCube Collaboration

R. Abbasi¹⁶, M. Ackermann⁶³, J. Adams¹⁷, S. K. Agarwalla^{39, a}, J. A. Aguilar¹⁰, M. Ahlers²¹, J.M. Alameddine²², S. Ali³⁵, N. M. Amin⁴³, K. Andeen⁴¹, C. Argüelles¹³, Y. Ashida⁵², S. Athanasiadou⁶³, S. N. Axani⁴³, R. Babu²³, X. Bai⁴⁹, J. Baines-Holmes³⁹, A. Balagopal V.^{39, 43}, S. W. Barwick²⁹, S. Bash²⁶, V. Basu⁵², R. Bay⁶, J. J. Beatty^{19, 20}, J. Becker Tjus^{9, b}, P. Behrens¹, J. Beise⁶¹, C. Bellenghi²⁶, B. Benkel⁶³, S. BenZvi⁵¹, D. Berley¹⁸, E. Bernardini^{47, c}, D. Z. Besson³⁵, E. Blaufuss¹⁸, L. Bloom⁵⁸, S. Blot⁶³, I. Bodo³⁹, F. Bontempo³⁰, J. Y. Book Motzkin¹³, C. Boscolo Meneguolo^{47, c}, S. Böser⁴⁰, O. Botner⁶¹, J. Böttcher¹, J. Braun³⁹, B. Brinson⁴, Z. Brisson-Tsavoussis³², R. T. Burley², D. Butterfield³⁹, M. A. Campana⁴⁸, K. Carloni¹³, J. Carpio^{33, 34}, S. Chattopadhyay^{39, a}, N. Chau¹⁰, Z. Chen⁵⁵, D. Chirkin³⁹, S. Choi⁵², B. A. Clark¹⁸, A. Coleman⁶¹, P. Coleman¹, G. H. Collin¹⁴, D. A. Coloma Borja⁴⁷, A. Connolly^{19, 20}, J. M. Conrad¹⁴, R. Corley⁵², D. F. Cowen^{59, 60}, C. De Clercq¹¹, J. J. DeLaunay⁵⁹, D. Delgado¹³, T. Delmeulle¹⁰, S. Deng¹, P. Desiati³⁹, K. D. de Vries¹¹, G. de Wasseige³⁶, T. DeYoung²³, J. C. Díaz-Vélez³⁹, S. DiKerby²³, M. Dittmer⁴², A. Domi²⁵, L. Draper⁵², L. Dueser¹, D. Durnford²⁴, K. Dutta⁴⁰, M. A. DuVernois³⁹, T. Ehrhardt⁴⁰, L. Eidenschink²⁶, A. Eimer²⁵, P. Eller²⁶, E. Ellinger⁶², D. Elsässer²², R. Engel^{30, 31}, H. Erpenbeck³⁹, W. Esmail⁴², S. Eulig¹³, J. Evans¹⁸, P. A. Evenson⁴³, K. L. Fan¹⁸, K. Fang³⁹, K. Farrag¹⁵, A. R. Fazely⁵, A. Fedynitch⁵⁷, N. Feigl⁸, C. Finley⁵⁴, L. Fischer⁶³, D. Fox⁵⁹, A. Franckowiak⁹, S. Fukami⁶³, P. Fürst¹, J. Gallagher³⁸, E. Ganster¹, A. Garcia¹³, M. Garcia⁴³, G. Garg^{39, a}, E. Genton^{13, 36}, L. Gerhardt⁷, A. Ghadimi⁵⁸, C. Glaser⁶¹, T. Glüsenkamp⁶¹, J. G. Gonzalez⁴³, S. Goswami^{33, 34}, A. Granados²³, D. Grant¹², S. J. Gray¹⁸, S. Griffin³⁹, S. Griswold⁵¹, K. M. Groth²¹, D. Guevel³⁹, C. Günther¹, P. Gutjahr²², C. Ha⁵³, C. Haack²⁵, A. Hallgren⁶¹, L. Halve¹, F. Halzen³⁹, L. Hamacher¹, M. Ha Minh²⁶, M. Handt¹, K. Hanson³⁹, J. Hardin¹⁴, A. A. Harnisch²³, P. Hatch³², A. Haungs³⁰, J. Häußler¹, K. Helbing⁶², J. Hellrung⁹, B. Henke²³, L. Hennig²⁵, F. Henningsen¹², L. Heuermann¹, R. Hewett¹⁷, N. Heyer⁶¹, S. Hickford⁶², A. Hidvegi⁵⁴, C. Hill¹⁵, G. C. Hill², R. Hmaid¹⁵, K. D. Hoffman¹⁸, D. Hooper³⁹, S. Hori³⁹, K. Hoshina^{39, d}, M. Hostert¹³, W. Hou³⁰, T. Huber³⁰, K. Hultqvist⁵⁴, K. Hymon^{22, 57}, A. Ishihara¹⁵, W. Iwakiri¹⁵, M. Jacquart²¹, S. Jain³⁹, O. Janik²⁵, M. Jansson³⁶, M. Jeong⁵², M. Jin¹³, N. Kamp¹³, D. Kang³⁰, W. Kang⁴⁸, X. Kang⁴⁸, A. Kappes⁴², L. Kardum²², T. Karg⁶³, M. Karl²⁶, A. Karle³⁹, A. Katil²⁴, M. Kauer³⁹, J. L. Kelley³⁹, M. Khanal⁵², A. Khatee Zathul³⁹, A. Kheirandish^{33, 34}, H. Kimku⁵³, J. Kiryluk⁵⁵, C. Klein²⁵, S. R. Klein^{6, 7}, Y. Kobayashi¹⁵, A. Kochocki²³, R. Koirala⁴³, H. Kolanoski⁸, T. Kontrimas²⁶, L. Köpke⁴⁰, C. Kopper²⁵, D. J. Koskinen²¹, P. Koundal⁴³, M. Kowalski^{8, 63}, T. Kozynets²¹, N. Krieger⁹, J. Krishnamoorthi^{39, a}, T. Krishnan¹³, K. Kruiswijk³⁶, E. Krupczak²³, A. Kumar⁶³, E. Kun⁹, N. Kurahashi⁴⁸, N. Lad⁶³, C. Lagunas Gualda²⁶, L. Lallement Arnaud¹⁰, M. Lamoureux³⁶, M. J. Larson¹⁸, F. Lauber⁶², J. P. Lazar³⁶, K. Leonard DeHoltan⁶⁰, A. Leszczyńska⁴³, J. Liao⁴, C. Lin⁴³, Y. T. Liu⁶⁰, M. Liubarska²⁴, C. Love⁴⁸, L. Lu³⁹, F. Lucarelli²⁷, W. Luszcza^{19, 20}, Y. Lyu^{6, 7}, J. Madsen³⁹, E. Magnus¹¹, K. B. M. Mahn²³, Y. Makino³⁹, E. Manao²⁶, S. Mancina^{47, e}, A. Mand³⁹, I. C. Mariş¹⁰, S. Marka⁴⁵, Z. Marka⁴⁵, L. Marten¹, I. Martinez-Soler¹³, R. Maruyama⁴⁴, J. Mauro³⁶, F. Mayhew²³, F. McNally³⁷, J. V. Mead²¹, K. Meagher³⁹, S. Mechbal⁶³, A. Medina²⁰, M. Meier¹⁵, Y. Merckx¹¹, L. Merten⁹, J. Mitchell⁵, L. Molchany⁴⁹, T. Montaruli²⁷, R. W. Moore²⁴, Y. Morii¹⁵, A. Mosbrugger²⁵, M. Moulai³⁹, D. Mousadi⁶³, E. Moyaux³⁶, T. Mukherjee³⁰, R. Naab⁶³, M. Nakos³⁹, U. Naumann⁶², J. Necker⁶³, L. Neste⁵⁴, M. Neumann⁴², H. Niederhausen²³, M. U. Nisa²³, K. Noda¹⁵, A. Noell¹, A. Novikov⁴³, A. Obertacke Pollmann¹⁵, V. O'Dell³⁹, A. Olivas¹⁸, R. Orsoe²⁶, J. Osborn³⁹, E. O'Sullivan⁶¹, V. Palusova⁴⁰, H. Pandya⁴³, A. Parenti¹⁰, N. Park³², V. Parrish²³, E. N. Paudel⁵⁸, L. Paul⁴⁹, C. Pérez de los Heros⁶¹, T. Pernice⁶³, J. Peterson³⁹, M. Plum⁴⁹, A. Pontén⁶¹, V. Poojyam⁵⁸, Y. Popovych⁴⁰, M. Prado Rodriguez³⁹, B. Pries²³, R. Procter-Murphy¹⁸, G. T. Przybylski⁷, L. Pyras⁵², C. Raab³⁶, J. Rack-Helleis⁴⁰, N. Rad⁶³, M. Ravn⁶¹, K. Rawlins³, Z. Rechav³⁹, A. Rehman⁴³, I. Reistoffer⁴⁹, E. Resconi²⁶, S. Reusch⁶³, C. D. Rho⁵⁶, W. Rhode²², L. Ricca³⁶, B. Riedel³⁹, A. Rifaie⁶², E. J. Roberts², S. Robertson^{6, 7}, M. Rongen²⁵, A. Rosted¹⁵, C. Rott⁵², T. Ruhe²², L. Ruohan²⁶, D. Ryckbosch²⁸, J. Saffer³¹, D. Salazar-Gallegos²³, P. Sampathkumar³⁰, A. Sandrock⁶², G. Sanger-Johnson²³, M. Santander⁵⁸, S. Sarkar⁴⁶, J. Savelberg¹, M. Scarnera³⁶, P. Schaile²⁶, M. Schaufel¹, H. Schieler³⁰, S. Schindler²⁵, L. Schlickmann⁴⁰, B. Schlüter⁴², F. Schlüter¹⁰, N. Schmeisser⁶², T. Schmidt¹⁸, F. G. Schröder^{30, 43}, L. Schumacher²⁵, S. Schwirn¹, S. Sclafani¹⁸, D. Seckel⁴³, L. Seen³⁹, M. Seikh³⁵, S. Seunarine⁵⁰, P. A. Seville Myhr³⁶, R. Shah⁴⁸, S. Shefali³¹, N. Shimizu¹⁵, B. Skrzypek⁶, R. Snihur³⁹, J. Soedingrekso²², A. Sogaard²¹, D. Soldin⁵², P. Soldin¹, G. Sommani⁹, C. Spannfellner²⁶, G. M. Spiczak⁵⁰, C. Spiering⁶³, J. Stachurska²⁸, M. Stamatikos²⁰, T. Stanev⁴³, T. Stezelberger⁷, T. Stürwald⁶², T. Stüttard²¹, G. W. Sullivan¹⁸, I. Taboada⁴, S. Ter-Antonyan⁵, A. Terliuk²⁶, A. Thakuri⁴⁹, M. Thiesmeyer³⁹, W. G. Thompson¹³, J. Thwaites³⁹, S. Tilav⁴³, K. Tollefson²³, S. Toscano¹⁰, D. Tosi³⁹, A. Trettin⁶³, A. K. Upadhyay^{39, a}, K. Upshaw⁵, A. Vaidyanathan⁴¹, N. Valtonen-Mattila^{9, 61}, J. Valverde⁴¹, J. Vandenbroucke³⁹, T. van Eeden⁶³, N. van Eijndhoven¹¹, L. van Rootselaar²², J. van Santen⁶³, F. J. Vara Carbonell⁴², F. Varsi³¹, M. Venugopal³⁰, M. Vereecken³⁶, S. Vergara Carrasco¹⁷, S. Verpoest⁴³, D. Veske⁴⁵, A. Vijai¹⁸, J. Villarreal¹⁴, C. Walck⁵⁴, A. Wang⁴, E. Warrick⁵⁸, C. Weaver²³, P. Weigel¹⁴, A. Weindl³⁰, J. Weldert⁴⁰, A. Y. Wen¹³, C. Wendt³⁹, J. Werthebach²², M. Weyrauch³⁰, N. Whitehorn²³, C. H. Wiebusch¹, D. R. Williams⁵⁸, L. Witthaus²², M. Wolf²⁶, G. Wrede²⁵, X. W. Xu⁵, J. P. Yañez²⁴, Y. Yao³⁹, E. Yildizci³⁹, S. Yoshida¹⁵, R. Young³⁵, F. Yu¹³, S. Yu⁵², T. Yuan³⁹, A. Zegarelli⁹, S. Zhang²³, Z. Zhang⁵⁵, P. Zhelnin¹³, P. Zilberman³⁹

¹ III. Physikalisches Institut, RWTH Aachen University, D-52056 Aachen, Germany

² Department of Physics, University of Adelaide, Adelaide, 5005, Australia

³ Dept. of Physics and Astronomy, University of Alaska Anchorage, 3211 Providence Dr., Anchorage, AK 99508, USA

⁴ School of Physics and Center for Relativistic Astrophysics, Georgia Institute of Technology, Atlanta, GA 30332, USA

⁵ Dept. of Physics, Southern University, Baton Rouge, LA 70813, USA

⁶ Dept. of Physics, University of California, Berkeley, CA 94720, USA

⁷ Lawrence Berkeley National Laboratory, Berkeley, CA 94720, USA

⁸ Institut für Physik, Humboldt-Universität zu Berlin, D-12489 Berlin, Germany

⁹ Fakultät für Physik & Astronomie, Ruhr-Universität Bochum, D-44780 Bochum, Germany

¹⁰ Université Libre de Bruxelles, Science Faculty CP230, B-1050 Brussels, Belgium

- ¹¹ Vrije Universiteit Brussel (VUB), Dienst ELEM, B-1050 Brussels, Belgium
- ¹² Dept. of Physics, Simon Fraser University, Burnaby, BC V5A 1S6, Canada
- ¹³ Department of Physics and Laboratory for Particle Physics and Cosmology, Harvard University, Cambridge, MA 02138, USA
- ¹⁴ Dept. of Physics, Massachusetts Institute of Technology, Cambridge, MA 02139, USA
- ¹⁵ Dept. of Physics and The International Center for Hadron Astrophysics, Chiba University, Chiba 263-8522, Japan
- ¹⁶ Department of Physics, Loyola University Chicago, Chicago, IL 60660, USA
- ¹⁷ Dept. of Physics and Astronomy, University of Canterbury, Private Bag 4800, Christchurch, New Zealand
- ¹⁸ Dept. of Physics, University of Maryland, College Park, MD 20742, USA
- ¹⁹ Dept. of Astronomy, Ohio State University, Columbus, OH 43210, USA
- ²⁰ Dept. of Physics and Center for Cosmology and Astro-Particle Physics, Ohio State University, Columbus, OH 43210, USA
- ²¹ Niels Bohr Institute, University of Copenhagen, DK-2100 Copenhagen, Denmark
- ²² Dept. of Physics, TU Dortmund University, D-44221 Dortmund, Germany
- ²³ Dept. of Physics and Astronomy, Michigan State University, East Lansing, MI 48824, USA
- ²⁴ Dept. of Physics, University of Alberta, Edmonton, Alberta, T6G 2E1, Canada
- ²⁵ Erlangen Centre for Astroparticle Physics, Friedrich-Alexander-Universität Erlangen-Nürnberg, D-91058 Erlangen, Germany
- ²⁶ Physik-department, Technische Universität München, D-85748 Garching, Germany
- ²⁷ Département de physique nucléaire et corpusculaire, Université de Genève, CH-1211 Genève, Switzerland
- ²⁸ Dept. of Physics and Astronomy, University of Gent, B-9000 Gent, Belgium
- ²⁹ Dept. of Physics and Astronomy, University of California, Irvine, CA 92697, USA
- ³⁰ Karlsruhe Institute of Technology, Institute for Astroparticle Physics, D-76021 Karlsruhe, Germany
- ³¹ Karlsruhe Institute of Technology, Institute of Experimental Particle Physics, D-76021 Karlsruhe, Germany
- ³² Dept. of Physics, Engineering Physics, and Astronomy, Queen's University, Kingston, ON K7L 3N6, Canada
- ³³ Department of Physics & Astronomy, University of Nevada, Las Vegas, NV 89154, USA
- ³⁴ Nevada Center for Astrophysics, University of Nevada, Las Vegas, NV 89154, USA
- ³⁵ Dept. of Physics and Astronomy, University of Kansas, Lawrence, KS 66045, USA
- ³⁶ Centre for Cosmology, Particle Physics and Phenomenology - CP3, Université catholique de Louvain, Louvain-la-Neuve, Belgium
- ³⁷ Department of Physics, Mercer University, Macon, GA 31207-0001, USA
- ³⁸ Dept. of Astronomy, University of Wisconsin—Madison, Madison, WI 53706, USA
- ³⁹ Dept. of Physics and Wisconsin IceCube Particle Astrophysics Center, University of Wisconsin—Madison, Madison, WI 53706, USA
- ⁴⁰ Institute of Physics, University of Mainz, Staudinger Weg 7, D-55099 Mainz, Germany
- ⁴¹ Department of Physics, Marquette University, Milwaukee, WI 53201, USA
- ⁴² Institut für Kernphysik, Universität Münster, D-48149 Münster, Germany
- ⁴³ Bartol Research Institute and Dept. of Physics and Astronomy, University of Delaware, Newark, DE 19716, USA
- ⁴⁴ Dept. of Physics, Yale University, New Haven, CT 06520, USA
- ⁴⁵ Columbia Astrophysics and Nevis Laboratories, Columbia University, New York, NY 10027, USA
- ⁴⁶ Dept. of Physics, University of Oxford, Parks Road, Oxford OX1 3PU, United Kingdom
- ⁴⁷ Dipartimento di Fisica e Astronomia Galileo Galilei, Università Degli Studi di Padova, I-35122 Padova PD, Italy
- ⁴⁸ Dept. of Physics, Drexel University, 3141 Chestnut Street, Philadelphia, PA 19104, USA
- ⁴⁹ Physics Department, South Dakota School of Mines and Technology, Rapid City, SD 57701, USA
- ⁵⁰ Dept. of Physics, University of Wisconsin, River Falls, WI 54022, USA
- ⁵¹ Dept. of Physics and Astronomy, University of Rochester, Rochester, NY 14627, USA
- ⁵² Department of Physics and Astronomy, University of Utah, Salt Lake City, UT 84112, USA
- ⁵³ Dept. of Physics, Chung-Ang University, Seoul 06974, Republic of Korea
- ⁵⁴ Oskar Klein Centre and Dept. of Physics, Stockholm University, SE-10691 Stockholm, Sweden
- ⁵⁵ Dept. of Physics and Astronomy, Stony Brook University, Stony Brook, NY 11794-3800, USA
- ⁵⁶ Dept. of Physics, Sungkyunkwan University, Suwon 16419, Republic of Korea
- ⁵⁷ Institute of Physics, Academia Sinica, Taipei, 11529, Taiwan
- ⁵⁸ Dept. of Physics and Astronomy, University of Alabama, Tuscaloosa, AL 35487, USA
- ⁵⁹ Dept. of Astronomy and Astrophysics, Pennsylvania State University, University Park, PA 16802, USA
- ⁶⁰ Dept. of Physics, Pennsylvania State University, University Park, PA 16802, USA
- ⁶¹ Dept. of Physics and Astronomy, Uppsala University, Box 516, SE-75120 Uppsala, Sweden
- ⁶² Dept. of Physics, University of Wuppertal, D-42119 Wuppertal, Germany
- ⁶³ Deutsches Elektronen-Synchrotron DESY, Platanenallee 6, D-15738 Zeuthen, Germany
- ^a also at Institute of Physics, Sachivalaya Marg, Sainik School Post, Bhubaneswar 751005, India
- ^b also at Department of Space, Earth and Environment, Chalmers University of Technology, 412 96 Gothenburg, Sweden
- ^c also at INFN Padova, I-35131 Padova, Italy
- ^d also at Earthquake Research Institute, University of Tokyo, Bunkyo, Tokyo 113-0032, Japan
- ^e now at INFN Padova, I-35131 Padova, Italy

Acknowledgments

The authors gratefully acknowledge the support from the following agencies and institutions: USA – U.S. National Science Foundation-Office of Polar Programs, U.S. National Science Foundation-Physics Division, U.S. National Science Foundation-EPSCoR, U.S. National Science Foundation-Office of Advanced Cyberinfrastructure, Wisconsin Alumni Research Foundation, Center for High Throughput Computing (CHTC) at the University of Wisconsin–Madison, Open Science Grid (OSG), Partnership to Advance Throughput Computing (PATH), Advanced Cyberinfrastructure Coordination Ecosystem: Services & Support (ACCESS), Frontera and Ranch computing project at the Texas Advanced Computing Center, U.S. Department of Energy-National Energy Research Scientific Computing Center, Particle astrophysics research computing center at the University of Maryland, Institute for Cyber-Enabled Research at Michigan State University, Astroparticle physics computational facility at Marquette University, NVIDIA Corporation, and Google Cloud Platform; Belgium – Funds for Scientific Research (FRS-FNRS and FWO), FWO Odysseus and Big Science programmes, and Belgian Federal Science Policy Office (Belspo); Germany – Bundesministerium für Forschung, Technologie und Raumfahrt (BMFTR), Deutsche Forschungsgemeinschaft (DFG), Helmholtz Alliance for Astroparticle Physics (HAP), Initiative and Networking Fund of the Helmholtz Association, Deutsches Elektronen Synchrotron (DESY), and High Performance Computing cluster of the RWTH Aachen; Sweden – Swedish Research Council, Swedish Polar Research Secretariat, Swedish National Infrastructure for Computing (SNIC), and Knut and Alice Wallenberg Foundation; European Union – EGI Advanced Computing for research; Australia – Australian Research Council; Canada – Natural Sciences and Engineering Research Council of Canada, Calcul Québec, Compute Ontario, Canada Foundation for Innovation, WestGrid, and Digital Research Alliance of Canada; Denmark – Villum Fonden, Carlsberg Foundation, and European Commission; New Zealand – Marsden Fund; Japan – Japan Society for Promotion of Science (JSPS) and Institute for Global Prominent Research (IGPR) of Chiba University; Korea – National Research Foundation of Korea (NRF); Switzerland – Swiss National Science Foundation (SNSF).